Sintering behavior and electrochemical performance of A-site deficient $Sr_xTi_{0.3}Fe_{0.7}O_{3-\delta}$ oxygen electrodes for solid oxide electrochemical cells

Hao Yang [a], Muhammad Bilal Hanif [a], Shan-Lin Zhang [a,b,**], Chang-Jiu Li [a], Cheng-Xin Li [a,*]

[a] State Key Laboratory for Mechanical Behavior of Materials, School of Materials Science and Engineering, Xi'an Jiaotong University, Xi'an, Shaanxi, China
[b] School of Chemical Engineering and Technology, Sun Yat-sen University, Zhuhai Campus, Zhuhai, Guangdong, 519082, China

ARTICLE INFO

ABSTRACT

$Sr(Ti_{0.3}Fe_{0.7})O_{3-\delta}$ (STF) materials with satisfactory stability and no rare-metal elements have attracted increasing research interest as oxygen electrodes of solid oxide electrochemical cells. However, STF-based electrodes are still limited by their modest catalytic activities at low temperatures. This can be improved by A-site deficiency of STF-based materials; however, data related to the influence of A-site deficiency of perovskite-oxide-based materials on sintering behavior and electrochemical performance are still lacking. Herein, porous electrodes with different $Sr_x(Ti_{0.3}Fe_{0.7})O_{3-\delta}$ compositions (x = 0.85–1) were prepared. The effects of A-site cation deficiency ratios and sintering temperatures on the microstructures and electrochemical performance of the as-obtained STF electrodes were investigated. Electrochemical performance was improved for A-site deficient $Sr_x(Ti_{0.3}Fe_{0.7})O_{3-\delta}$. For $Sr_{0.9}(Ti_{0.3}Fe_{0.7})_{3-\delta}$ electrode material sintered at 1050 °C, the lowest polarization resistance measured at 700 °C was ~0.14 Ω·cm² but increased at higher x values. At sintering temperatures above 1050 °C, the sintering diffusion occurred, where the electrolyte diffused through the deficient electrodes to form a dense layer at the electrode/electrolyte interface. On the other hand, although the presence of such diffused dense layer did not have significant effect on the electrochemical performance of the cells, it could be prevented by using lower sintering temperatures (≤1000 °C) to avoid possible negative effects on comprehensive performance. For the electrode obtained at x = 0.9 and sintered at 1000 °C, the overall polarization resistance was recorded as 0.099 Ω·cm² at 700 °C. In sum, these findings look promising for future research.

1. Introduction

Solid oxide electrochemical cells (SOCs) are efficient energy storage devices, which can directly convert chemical energy into useable electrical energy (solid oxide fuel cell mode) [1,2] and they store electricity as a chemical fuel (solid oxide electrolysis cell mode) via electrochemical reactions [3,4]. SOCs are advantageous over the traditional energy conversion systems in terms of high efficiency, reliability, modularity, adaptability, environmental-friendliness and sustainability [5]. Nevertheless, fuel-cell technology still suffers from several issues, in particular, at the high operating temperatures (up to 800 °C) that must be lowered [1,6–8]. When the operating temperatures are below 700 °C, the electrochemical performance of SOCs undergoes rapid deterioration due to the decline in the catalytic activities of the electrodes [9]. For instance, some studies have shown that oxygen electrodes (oxygen reduction reaction in fuel cell mode [10,11] and oxygen evolution reaction in electrolysis mode) have worst catalytic activities at low operating temperatures when compared to fuel electrodes [3,6–8]. Therefore, high-activity oxygen electrode materials have been explored to reduce the operating temperatures of SOCs [12,13].

Iron doped strontium titanates ($Sr(Ti_{1-x}Fe_x)O_{3-\delta}$, STF) are potential materials for oxygen electrodes of SOCs [14–17]. STF electrodes are advantages in terms of high stability, low-cost, and absence of rare earth elements. Moreover, they can be used as both fuel and oxygen electrodes [18–22,38–42]. However, the catalytic performances of STF materials are still poor at low temperatures (<700 °C), commonly caused by the Sr segregation on the electrode surface [23]. Therefore, further improvement in catalytic performance of STF electrodes is required before their widespread applications. In this view, Ni et al. investigated various stoichiometries of $Sr_{1-x}Ti_{0.3}Fe_{0.6}Ni_{0.1}O_{3-\delta}$ to figure out stable, efficient,

and cost-competitive oxygen electrodes based on $Sr_{0.95}Ti_{0.3}Fe_{0.6}Ni_{0.1}O_{3-\delta}$ for SOCs. They noticed that A-site cation deficiency could improve the electrochemical performance and restrain Sr segregation effectively [24–26]. However, systematic studies dealing with the influence of A-site deficient state on sintering characteristics and electrochemical performance of STF-based electrode have not been reported so far. On the other hand, the sintering characteristics of the electrodes are of great significance for optimizing the microstructure and performance.

We previously investigated different Ti-doped STFs and found that $Sr(Ti_{0.3}Fe_{0.7})O_{3-\delta}$ showed the best performance in oxygen electrodes with various Ti and Fe compositions [22]. Herein, the performances of electrodes prepared with $Sr_xTi_{0.3}Fe_{0.7}O_{3-\delta}$ (x = 1, 0.95, 0.9, and 0.85) followed by sintering at 1100, 1050, and 1000 °C, respectively, were studied in terms of phase structure and electronic conductivity. This was particularly performed by analyzing the effects of different A-site deficiency ratios and sintering temperatures on the microstructures and electrochemical performance of STF electrodes. The results indicate an improvement in the electrochemical performance with the increase in ratio of A-site deficiency. The lowest polarization resistance was recorded with $Sr_{0.9}(Ti_{1-x}Fe_x)O_{3-\delta}$ electrode. Remarkably, noteworthy, when the STF cell with A-site deficiency is sintered at high temperatures, the sintering diffusion occurs, where the electrolyte diffuses through the deficient electrodes to form a dense layer at the electrode/electrolyte interface. There is no evidence whether the formation of this continuous dense layer affects the performance of the electrode, but herein this phenomenon was recorded for the first time.

2. Experimental

2.1. Materials synthesis and cell fabrication

$Sr_x(Ti_{0.3}Fe_{0.7})O_{3-\delta}$ powders (with x = 1, 0.95, 0.9, and 0.85) were synthesized by the sol–gel method. To this end, $Sr(NO_3)_2 \cdot 6H_2O$ (99.5%), $Fe(NO_3)_3 \cdot 9H_2O$ (98.5%), ethylene glycol (EG, 99%), and citric acid (99.5%) obtained from Sinopharm Chemical Reagent Co. Ltd. and tetrabutyl titanate (98%) from Aladdin were used as starting materials. The nitrate mixture was obtained by dissolving stoichiometric amounts of $Sr(NO_3)_2 \cdot 6H_2O$ and $Fe(NO_3)_3 \cdot 9H_2O$ in deionized water to yield solution A. Next, a stoichiometric amount of tetrabutyl titanate was dissolved in dehydrating alcohol to yield an alcoholic solution B. Further, solutions A and B were mixed under constant stirring to form a uniform mixture, which was followed by the addition of citric acid and EG. The molar ratios of EG to metal and citric to metal were 1.5:1 and 2:1, respectively. The obtained homogeneous solution was then heated in a water bath at 80 °C to yield a viscous gel of metal-citrate complex after evaporation of water and alcohol solvents. Finally, the as-obtained viscous gels were dried at 150 °C to form foam-like dried gels, which were then calcined at 1050 °C for 5 h in the air followed by ball-milling in ethanol for another 12 h and drying.

The symmetrical cells were assembled using $Ce_{0.9}Gd_{0.1}O_{2-\delta}$ (GDC) electrolytes. The sintered GDC pellets (1450 °C/5 h) had a diameter 13.5 mm and thickness of ~0.8–1.0 mm. STF inks were prepared in a three-roll mill by mixing STF powders with a binder (V-737, Heraeus) at a weight ratio of 1 : 1.2. Next, the inks were screen printed on both sides of electrode pellets followed by firing at 1100, 1050, and 1000 °C for 3 h. The resulting electrodes possessed a thickness of 15–20 μm and an area of 0.28 cm^2.

2.2. Materials characterization

The phase structures of STF powders were identified by X-ray diffraction (XRD, Bruker D8 ADVANCE). To investigate the possible reactions between the A-site deficient STF electrodes and GDC electrolytes, the STF and GDC powders were mixed (50%: 50%) and pressed into pellets followed by firing at 1100 °C. The phase structures of fired pellets were determined by XRD.

For conductivity measurements, dense bar-shaped pellets (dimension ~5 mm × 5 mm × 25 mm) were prepared by sintering at 1200 °C for 5 h. The electrical conductivity was measured by the four-probe DC method on an electrochemical workstation (Solartron SI 1260/1287).

The microstructures were characterized by scanning electron microscopy (SEM, Hitachi S3400). The element distributions were analyzed by X-ray energy dispersive spectroscopy (EDS).

2.3. Electrochemical measurements

To facilitate the current collection, silver grids (Heraeus Inc. Pennsylvania) were first screen printed on both sides of the cells. The electrochemical impedance spectroscopy (EIS) measurements were then conducted at 600–800 °C on a Solartron SI 1260/1287 impedance analyzer. The measurements were performed under the following conditions: ambient air open-circuit voltage (OCV) current of 20 mV AC, and frequency range from 0.1 Hz to 100 k Hz. The EIS tests were first performed at 800 °C followed by a decline in temperature with the final test at 600 °C.

3. Results and discussions

3.1. Basic properties of $Sr_x(Ti_{0.3}Fe_{0.7})O_{3-\delta}$: phase composition and conductivity

The XRD patterns of the as-obtained $Sr_x(Ti_{0.3}Fe_{0.7})O_{3-\delta}$ powders are shown in Fig. 1(a). Only representative peaks of cubic perovskite structure are observed, indicating that the impurity phases were not formed. The micro-area XRD patterns of the as-prepared STF powders under various parameters in the 2θ range of 32 °–33° are displayed in Fig. 1(b). The diffraction angle of the main peak in deficiency-free powder is located at about 32.66°, consistent with the literature report [27]. As the ratio of defects increases, the diffraction angle of the main diffraction peak shows a gradual decrease. At a deficiency ratio of 15%, the diffraction angle reduces to 32.58°. This confirms the introduction of vacancies in the perovskite structure, similar to the case with other STF-based and perovskite materials with introduced A-site deficient [24].

Fig. 1(c-d) indicate that the A-site deficient STF illustrates no reaction with GDC to form the third phase. Unlike the phase structure of STF powder, the main peak diffraction angle of STF in STF-GDC pellets shows no change with the change in the ratio of A-site deficient STF powders. The reason for this will be discussed later.

The total electrical conductivity of STF bulks in the air is mainly due to the electronic conductivity. With the decrease in the Sr content, the conductivity gradually decreases (Fig. 2) due to the progressive delocalization of atomic levels and the rise in bandwidth [28]. All the materials obtained at various compositions exhibited similar temperature dependence. The maximum electrical conductivities at 400–600 °C ranged from 6 S cm^{-1} for x = 0.85–11.86 S cm^{-1} for x = 1. The latter value at x = 1 agrees reasonably well with prior published reports [22]. Therefore, the conductivities of STF materials were lower than the values of some other perovskite oxygen electrodes. However, they should suffice for applications in thin (~15–20 μm) electrode functional layers. For current collectors, it may be desirable to use higher-conductivity materials.

3.2. Electrode microstructure

Fractured cross-sectional SEM images of the as-prepared STF electrodes are depicted in Fig. 3(a)-(f) and Fig. S1(a)–(f). The thickness of all STF electrodes was estimated to be ~20 μm. Moreover, all electrodes were well bonded with the GDC electrolyte. For comparative analysis, Fig. 3(a)–(f) show representative polished cross-sectional SEM images of STF electrodes, consisting of the deficiency-free electrode and typical
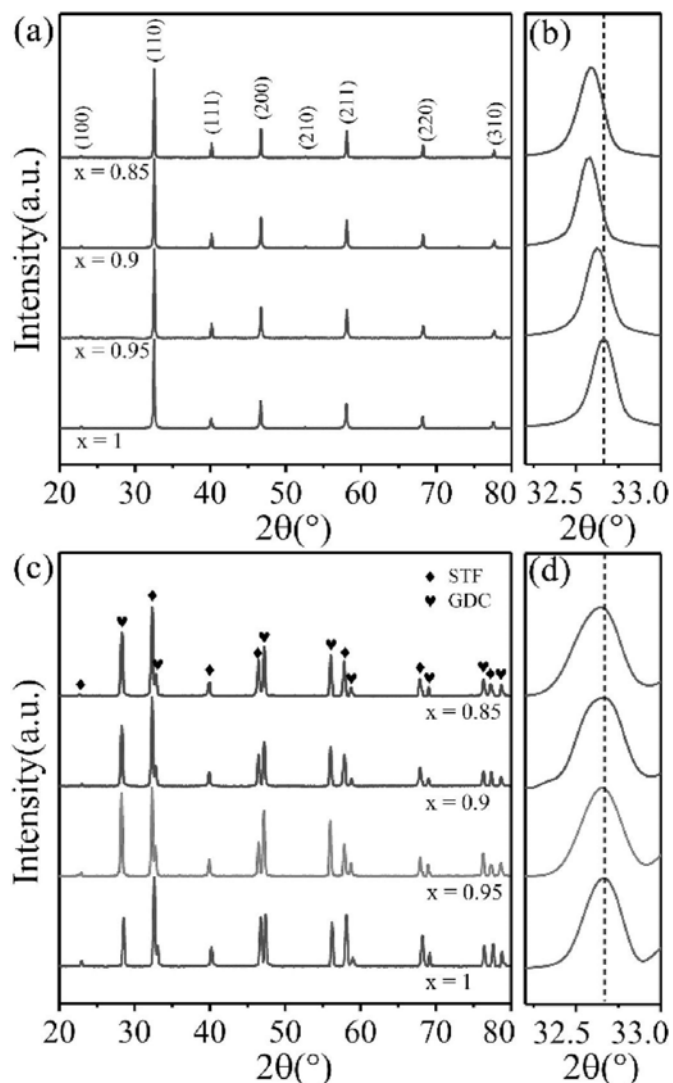
Fig. 1. XRD patterns of: **(a)** as-obtained STF powders, **(b)** main peak region of STF powders, **(c)** STF-GDC pellets sintered at 1100 °C for 3 h, and **(d)** main peak region of STF-GDC pellets sintered at 1100 °C for 3 h.

deficient electrode obtained at x = 0.9 followed by sintering at different temperatures. For x = 1, the electrode particles have regular spherical shapes, similar to those reported in our previous studies [22,28,29]. The size scale significantly increases with sintering temperature, and bonding between particles gets enhanced dramatically. In contrast, the A-site deficient electrodes look different at the same sintering temperature. First, the electrode particles are relatively larger with irregular morphologies. This may be attributed to the deficiency that leads to a decrease in melting point values of the materials [30]. More importantly, a dense layer is formed at the electrode/electrolyte interface at sintering temperature greater than 1050 °C. Moreover, the thickness of the dense layer reached ~4 μm when deficient electrodes were sintered at 1100 °C. Furthermore, the thickness of the porous part of the electrode declines from ~20 μm to ~15 μm. Fig. S1 demonstrates that other ratios of deficient electrode materials depict similar tendencies. The formation mechanism of the dense layer at the electrode/electrolyte interface will be discussed later.

Cross-sectional SEM images of representative fracture of different electrodes sintered at 1050 °C and 1000 °C are presented in Figs. S2 and S3. The STF electrode exhibits an expected porous microstructure at the sintering temperature of 1050 °C (Fig. S2). The particles deposited on the electrode prepared at x = 1 are relatively regular and spherical in
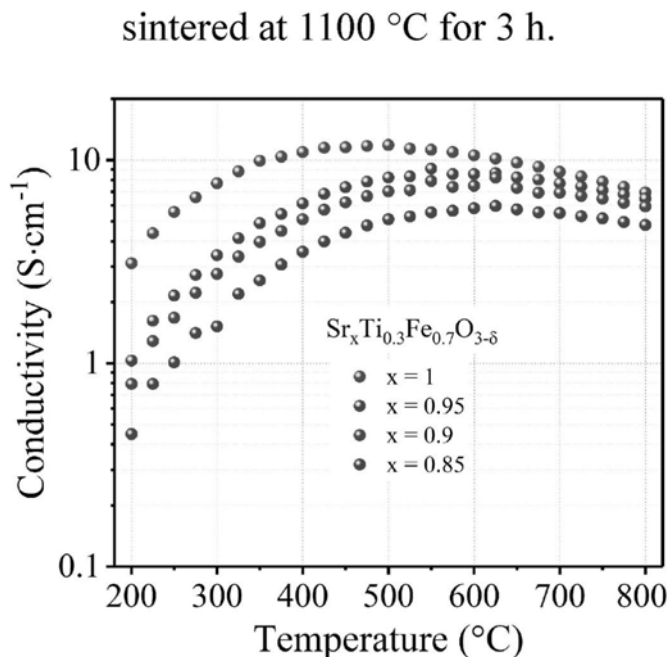

Fig. 2. Total conductivity values of different STF bulks.

shape (Fig. S2(a)). The electrodes obtained at x = 0.95 (Fig. S2(b)), x = 0.9 (Fig. S2(c)), and x = 0.85 (Fig. S2(d)) display porous microstructures with well-connected electrode particles. Moreover, the porosity of the deficient sample is significantly larger than that obtained at x = 1. The deficiency-free electrode displays finer particles at a decreased sintering temperature of 1000 °C; however, the deficient electrodes shows a limited number of visible large particles together with small particles attached to its surface (Fig. S3).

The variation trends in STF porosity (Fig. 4 (a)) and specific surface area (Fig. 4(b)) as a function of x, along with images obtained from the sintered stereological analysis are presented in Fig. 3 and Fig. S1. Noteworthy, the porosity decreases with sintering temperature from ~45% (sintered at 1000 °C) to ~ 28% (sintered at 1100 °C), consistent with the enhancement in recorded particle size. Furthermore, the defect ratio at the same sintering temperature shows little influence on porosity. Such trends can be understood in terms of the decreasing melting point with increasing deficiency ratio [30]. However, the specific surface area decreases not only with the sintering temperature, but also by introducing defects. For instance, the value at sintering temperature of 1050 °C declines from 3.84 μm^{-1} (x = 1) to 1.89 μm^{-1} (x = 0.95). This is attributed to the appearance of larger particles inside the electrode upon the introduction of deficient state (Fig. 3).

3.3. Dense diffusion layer analysis

According to XRD data shown in Fig. 1(c), the STF-GDC pellets sintered at 1100 °C for 3 h did not react to form the third phase. Thus, the dense layer observed in Fig. 3 was only caused by the diffusion of electrolyte to the electrode. As a result, EDS line scanning was used to further analyze the thickness of the dense layer. To this end, at least 10 different regions were analyzed in each sample to obtain the average value. Typical EDS line scans of Sr, Ti, Fe, and Ce and Gd elements across the regions marked in Fig. 5(a) (x = 0.9 sintered at 1000 °C), Fig. 5(b) (x = 0.9 sintered at 1100 °C) and Fig. 5(c) (x = 1 sintered at 1100 °C) are provided in Fig. 5(d)-5(f), respectively. For the electrode obtained at x = 0.9 followed by sintering at 1000 °C, the element diffusion thickness was estimated to be ~1.5 μm and no visible dense layers were observed in the microstructure (Fig. 5(d)). This was caused by normal diffusion between materials during sintering, similar to the diffusion taking place
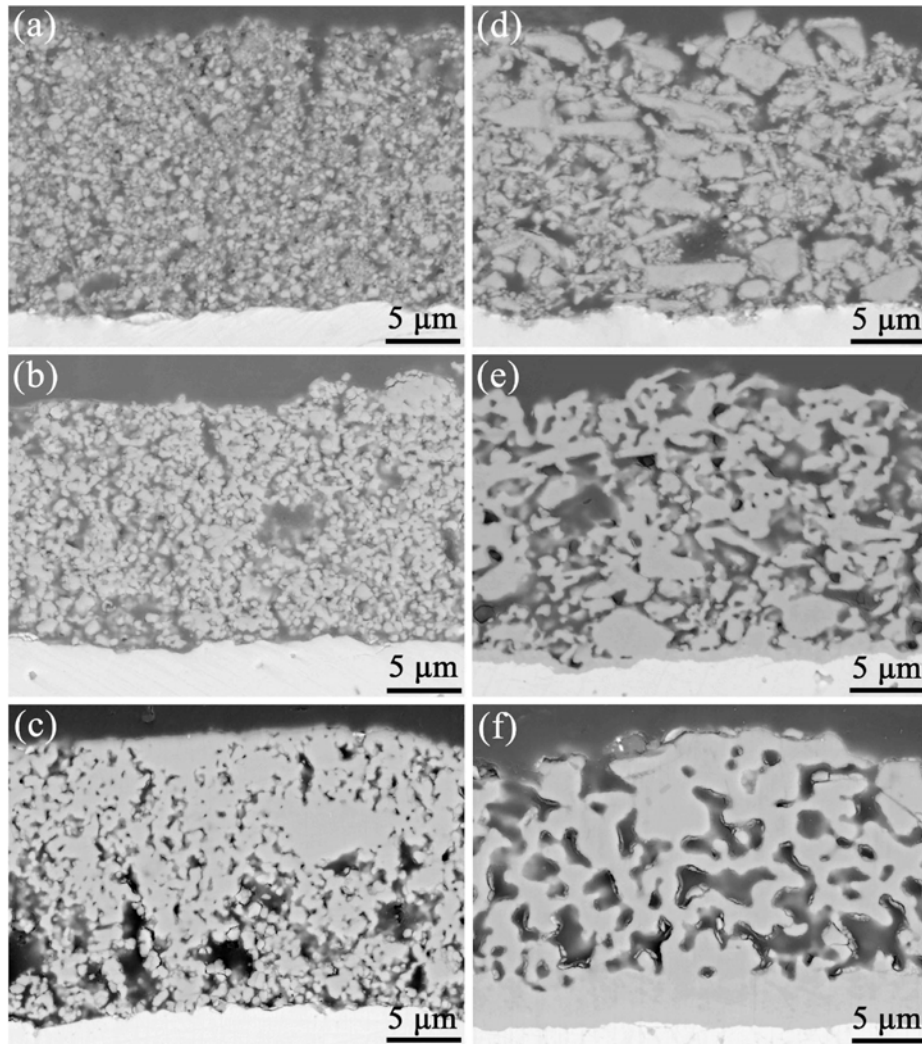
Fig. 3. Polished cross sectional SEM images of STF electrodes fired at different temperatures for x = 1 (**(a)** 1000 °C, **(b)** 1050 °C, and **(c)** 1100 °C); and x = 0.9 (**(d)** 1000 °C, **(e)** 1050 °C, and **(f)** 1100 °C).
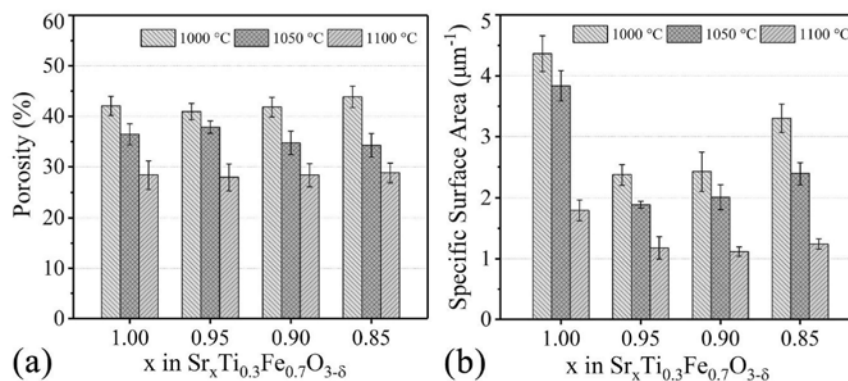
Fig. 4. (a) Porosity and **(b)** specific surface area obtained from 2D image analysis of different STF electrodes.

during sintering between $La_{1-x}Sr_xCo_{1-y}Fe_yO_{3-\delta}$ (LSCF) and $Ce_{0.9}Gd_{0.1}O_{2-\delta}$ (GDC) [31–33] or $La_{1-x}Sr_xMnO_3$ (LSM) and yttria-stabilized zirconia (YSZ) [34–36]. For the electrode obtained at x = 0.9 followed by sintering at 1100 °C (Fig. 5(e)), the diffusion layer reaches ~ 5 μm. Comparative analysis indicates that the thickness of the diffusion layer in the electrode obtained at x = 1 is only 1.5 μm even at sintering

temperature of 1100 °C. This looks similar to the deficient electrodes sintered at 1000 °C. Fig. S4 displays similar results recorded for other deficient samples.

SEM images showing the thickness of dense layers of as-prepared cells are displayed in Fig. 6(a). With the increase in the sintering temperature, the dense layer enhances. For instance, the dense layer
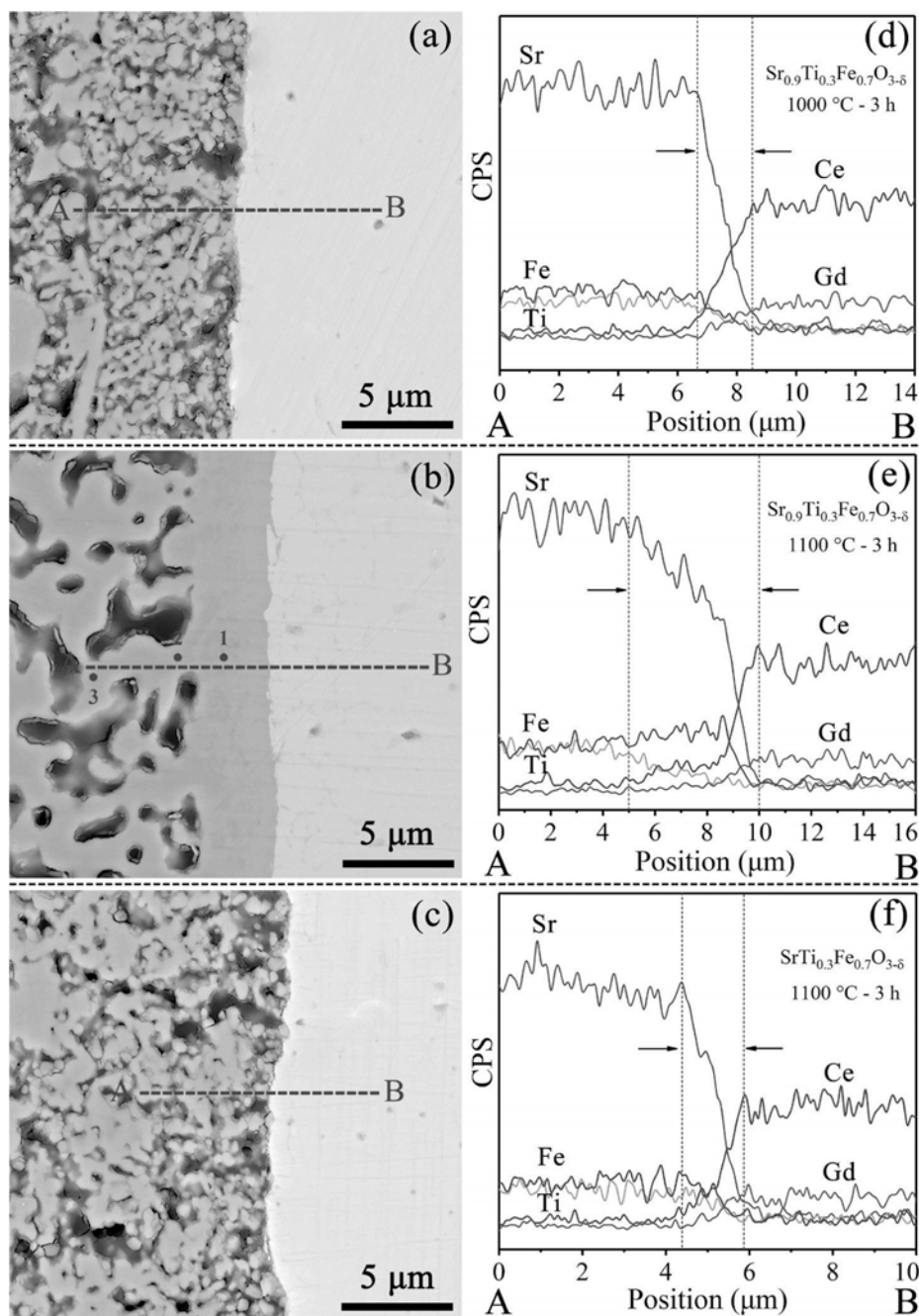
Fig. 5. Microstructure of a polished cross-section of STF: **(a)** x = 0.9 sintered at 1000 °C, **(b)** x = 0.9 sintered at 1100 °C, and **(c)** x = 1 sintered at 1100 °C, **(d)**, **(e)**, and **(f)** EDS elemental line scans corresponding to **(a)**, **(b)** and **(c)**, respectively.

thickness of all deficient electrodes increases from ~1 to ~3.8 μm with the increase in the sintering temperature from 1050 °C to 1100 °C. Moreover, the increment in the ratio of deficient electrode leads to a slight enhancement in the thickness of the dense layer.

The EDS line scan measurements of thicknesses of diffusion layers of electrodes obtained with different defects at various sintering temperatures are presented in Fig. 6(b). The diffusion layer thickness of the deficiency-free sample changes slightly with the sintering temperature, and the element diffusion is less than 1.5 μm. Comparative analysis indicates that the increase in sintering temperature leads to a significant enhancement in the diffusion layer of deficient samples. For example, the value of the electrode obtained at x = 0.9 followed by sintering at 1000 °C is ~1.5 μm, which increases to ~5 μm when the electrode is sintered at 1100 °C. Furthermore, the increment in the ratio of the

deficient electrode leads to a slight improvement in the thickness of the diffusion layer. For instance, the thickness of the electrode obtained x = 0.95 is recorded as ~4.7 μm, and increases to ~5.1 μm for the electrode obtained at x = 0.85 followed by sintering at 1100 °C. Noteworthy, at a sintering temperature of 1000 °C, the element diffusion layer of each parameter electrode is about 1 μm. As a result, element diffusion hardly occurs at sintering temperatures below 1000 °C. Compared to Fig. 6(a), the thickness of the diffusion layer is slightly greater than that of the dense layer under the same conditions.

The atomic percentages of elements determined by EDS point scanning at different positions in the dense layer shown in Fig. 5(b) are listed in Table 1. Notably, point 1 represents the distribution of various elements in the middle of the dense layer, point 3 shows the distribution of various elements in a distant location from the dense layer, and point 2
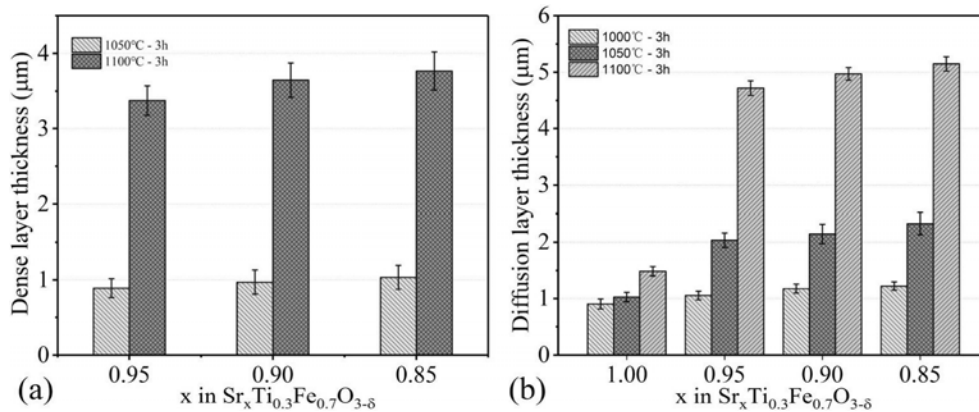
Fig. 6. Thickness of the **(a)** dense layer and **(b)** diffusion layer of electrodes obtained with different defects at various sintering temperatures.

Table 1
EDS point scanning of the atomic percentage of each element at different positions in the dense layer marked in Fig. 5(b).

Position	(Sr + Ce + Gd)/(Fe + Ti) (%)	(Ce + Gd) (%)
1	98.35	12.17
2	94.22	5.43
3	92.06	0.98

refers to the area between points 1 and 3. The sum of the atomic percentages of Ce and Gd at point 1 in the center of the dense layer was estimated to be 12.17%, while that of Ce and Gd at point 3 was 0.98%. This indicates that the electrolyte diffuses into the electrode. At point 1, the ratio of the sum of atomic percentages of Sr, Ce, and Gd to that of Ti and Fe is about 98.35%, while this ratio is about 92.06 %at point 3. Therefore, the diffusion of Ce and Gd elements fills the deficient A-site in

the electrode structure.

The formation of a continuous dense layer at the interfacing electrode/electrolyte at sintering temperatures above 1050 °C of A-site deficient STF electrodes results from the combined effect of many factors. First, the electrode with deficiency possesses lowered melting point and higher surface activity. Accordingly, the formation mechanism of the dense layer was proposed based on the sintering diffusion. Fig. S3(b-d) demonstrate that electrodes prepared by the sol-gel method possess numerous irregular small particles with a rough electrolyte surface. Thus, some fine particles on the electrode are in contact with local protrusions on the electrolyte surface and accelerate the sintering process. Such a process is significantly affected by the sintering temperature (Fig. 3(d–f)). In other words, the increase in sintering temperature gradually enhances the thickness of the dense layer. As indicated by the micro-region XRD results of STF-GDC pellets (Fig. 1(d)), the main peak of STF displays no shifting after sintering at 1100 °C for 3 h. This
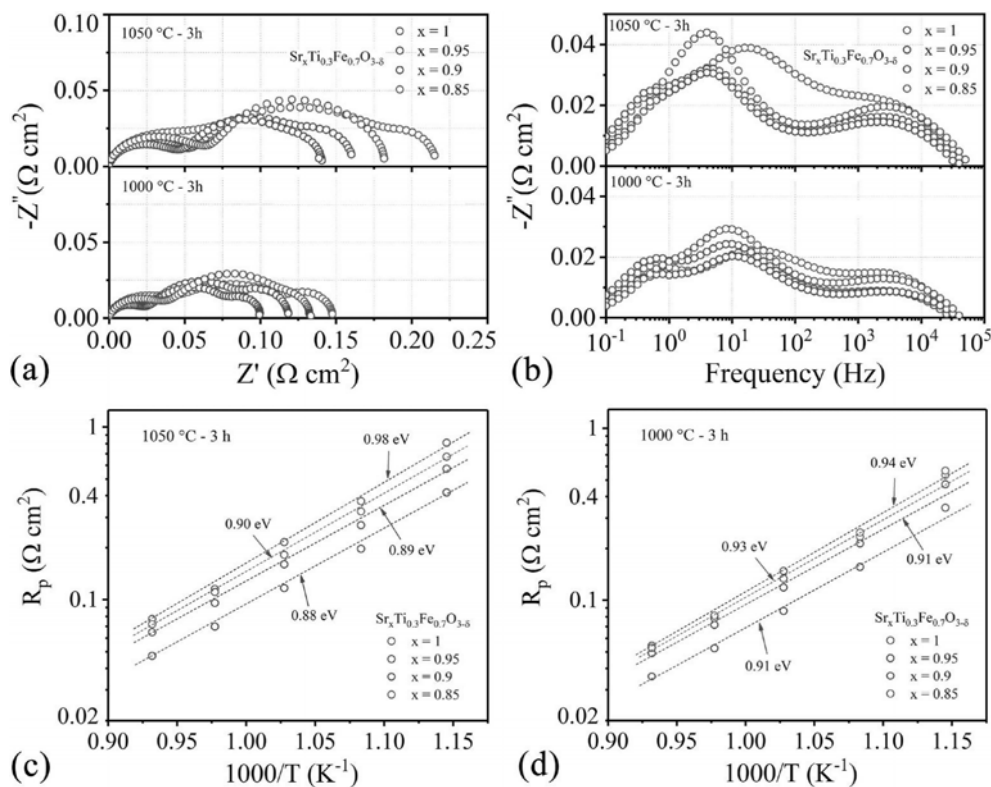

Fig. 7. Typical **(a)** Nyquist and **(b)** Bode plots measured at 700 °C. The high-frequency intercepts in the data are set to zero to better compare the polarization arcs. Arrhenius plots of the total electrode polarization resistance sintered at **(c)** 1050 °C and **(d)** 1000 °C measured from the EIS fitting results.

confirms the vanishing of the vacancy in STF lattice due to the migration of Ce and Gd atoms toward the vacancy in STF lattice. The latter can further be confirmed by the atomic percentage of each element in the dense layer (Table 1).

3.4. Electrode characteristics

Typical Nyquist and Bode plots of STF symmetric cells sintered at 1000 °C and 1050 °C and then measured in air at 700 °C by EIS are displayed in Fig. 7(a) and (b). As expected for such thickness of electrolyte, the high-frequency real-axis intercepts of impedance arcs are all within a range of ~0.7–0.85 $\Omega \cdot cm^2$ at 700 °C. As a result, the high-frequency intercepts are all set to zero in the Nyquist plots to clearly show the changes in the polarization responses. For the deficiency-free electrode sintered at 1050 °C, the R_p value was determined to be 0.21 $\Omega \cdot cm^2$. The increase in the ratio of deficient state reduces the overall polarization resistance, with the maximum decrease occurring at deficiency ratios between 0 and 10%. For the electrode obtained at x = 0.9, the overall polarization resistance is recorded as 0.14 $\Omega \cdot cm^2$, thereby reaching a minimum value. Further increase in x to 15% leads to an increase in the polarization resistance to 0.16 $\Omega \cdot cm^2$. The Bode plot shows a board diffusion response at frequencies ranging from ~1 to 10,000 Hz, and diminishing as x declines to 0.9. The high-frequency (1000–10,000 Hz) polarization response decreases with the ratio of deficient sites, similar to the trend registered in the middle-frequency range (1–1000 Hz). With the introduction of deficient sites, the dominant polarization response decreased from ~30 Hz to ~5 Hz. Further decrease in x to 0.85 resulted in the increase in the electrode response in both middle-frequency and high-frequency regions. However, the deficient feature exhibited little effect on the electrode response at low frequencies due to gas diffusion as well as the same porosity of all electrodes at the same sintering temperature. The decline in sintering temperature to 1000 °C resulted in a reduction in polarization resistances of all electrodes. Nevertheless, the regularity is consistent among all STF electrodes sintered at 1050 °C.

The variation in total R_p obtained from the fitting data as a function of the inverse temperature of all electrodes, sintered at 1050 °C and 1000 °C, is displayed in Fig. 7(c) and (d). The above-discussed variation trend of R_p versus the ratio of the deficiency at 700 °C is still relevant. At all sintering temperatures, R_p declines to a minimum at x = 0.9, and then increases with x. The Rp value of the electrode obtained at x = 0.9 reaches the lowest value of ~0.099 $\Omega \cdot cm^2$ at 700 °C.

The activation energy (E_a) values were calculated from linear fits of ln (R_p) vs. 1/T. Fig. 7(c) and (d) illustrate that the E_a of deficient-free sample (0.98 eV) is close to the value reported in our previous study (1.04 eV) [22,28,37]. A reduction in x from 1 to 0.9 leads to a decrease in E_a. However, further decline in x to 0.85 enhances E_a. Noteworthy, that the decrease in E_a value is helpful for enhancing the low-temperature performance of the electrodes.

In order to further evaluate the effect of dense layer on the electrochemical performance, Fig. 8 presents the comparative analysis of the total Rp value versus the ratio of A-site deficient electrodes sintered at 1050 °C and 1000 °C obtained from Fig. 7(a). Comparative study was carried out because there was a diffused dense layer at the electrode/electrolyte interface for samples sintered at 1050 °C, while no obvious diffusion layer was found for samples sintered at 1000 °C. Fig. 8 demonstrates that the increase in the ratio of deficiency from x = 1 to x = 0.9 leads first to a decline in the overall polarization resistance followed by an enhancement as x further diminishes. Moreover, the Rp for the sample sintered at 1000 °C is slightly lower than that of the sample sintered at 1050 °C. However, it was difficult to obtain a conclusion that the dense diffusion layer was responsible for increasing the Rp in present study because the samples sintered at 1050 °C exhibited a slightly lower porosity and specific surface area. For example, there was also a slight Rp decrease for x = 1 samples while both of them did not have dense diffusion layers.
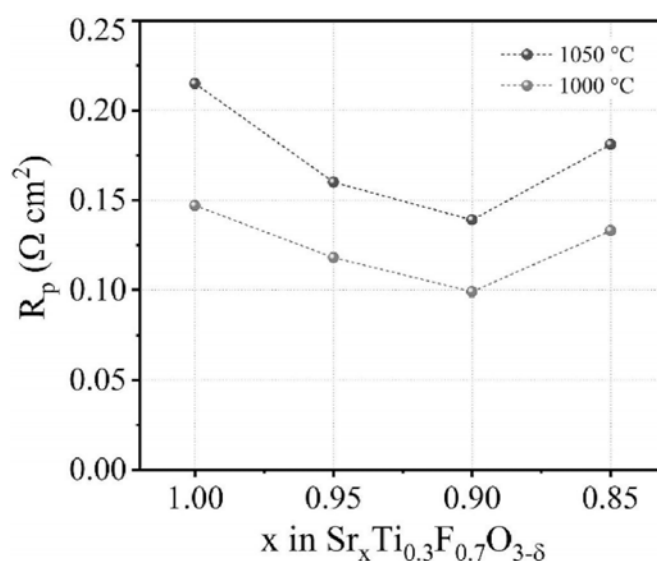

Fig. 8. R_p of symmetric cells at 700 °C obtained from the EIS results.

4. Conclusions

Porous $Sr_x(Ti_{0.3}Fe_{0.7})O_{3-\delta}$ electrodes with different compositions of x (from 0.85 to 1) were successfully prepared. The effects of A-site deficient ratios and sintering temperatures on the microstructure and electrochemical performance of the as-obtained STF electrodes were systematically investigated. The following conclusions can be drawn:

1. Electrode performance was improved and directly influenced by increased defect rates at same sintering temperature. Maximum increase in electrode performance was reported with 10% defect rate whereas significantly declined with increased defect rates.
2. The electrode with the same defect parameters displayed relatively well comprehensive performance when sintered at 1000 °C, the electrode obtained at x = 0.9 showed the best comprehensive performance, and the overall polarization resistance was recorded as 0.099 $\Omega \cdot cm^2$ at 700 °C.
3. When the STF cells with A-site deficiency are sintered at high temperatures, the sintering diffusion occurs, where the electrolyte diffuses through electrodes to form a dense layer at the electrode/electrolyte interface. The higher the sintering temperature, the more intense the diffusion phenomenon. When the sintering temperature was 1100 °C, the thickness of the dense layer reached ~4 μm, and that of the diffusion layer reached ~5 μm.
4. It was difficult to obtain the conclusion that the dense diffusion layer was responsible for increasing the Rp in present study because the samples sintered at 1050 °C exhibited a slightly lower porosity and specific surface area. However, this layer can be avoided by reducing the sintering temperature to yield better comprehensive performance.

Declaration of competing interest

The authors declare that they have no known competing financial interests or personal relationships that could have appeared to influence the work reported in this paper.

Acknowledgements

Appendix A. Supplementary data

Supplementary data to this article can be found online at https://doi.org/10.1016/j.ceramint.2021.05.235.

References

[1] B.C.H. Steele, A. Heinzel, Nature 414 (2001) 345–352.
[2] E.D. Wachsman, C.A. Marlowe, K.T. Lee, Energy Environ. Sci. 5 (2012) 5498–5509.
[3] C. Graves, S.D. Ebbesen, S.H. Jensen, S.B. Simonsen, M.B. Mogensen, Nat. Mater. 14 (2015) 239–244.
[4] D.M. Bierschenk, J.R. Wilson, S.A. Barnett, Energy Environ. Sci. 4 (2011) 944–951.
[5] S.C. Singhal, Solid State Ionics 135 (2000) 305–313.
[6] C. Duan, D. Hook, Y. Chen, J. Tong, R. O'Hayre, Energy Environ. Sci. 10 (2017) 176–182.
[7] A. Jun, J. Kim, J. Shin, G. Kim, ChemElectroChem 3 (2016) 511–530.
[8] Y. Chen, W. Zhou, D. Ding, M. Liu, F. Ciucci, M. Tade, Z. Shao, Advanced Energy Materials 5 (2015).
[9] C. Xia, Y. Lang, G. Meng, Fuel Cell. 4 (2004) 41–47.
[10] B.C.H. Steele, Solid State Ionics 129 (2000) 95–110.
[11] T.L. Simonenko, N.P. Simonenko, P.Y. Gorobtsov, I.S. Vlasov, V.R. Solovey, A. V. Shelaev, E.P. Simonenko, O.V. Glumov, N.A. Melnikova, M.G. Kozodaev, A. M. Markeev, A.A. Lizunova, I.A. Volkov, V.G. Sevastyanov, N.T. Kuznetsov, J. Colloid Interface Sci. 588 (2021) 209–220.
[12] L. Fan, B. Zhu, P.-C. Su, C. He, Nanomater. Energy 45 (2018) 148–176.
[13] Y.-L. Huang, A.M. Hussain, E.D. Wachsman, Nanomater. Energy 49 (2018) 186–192.
[14] S. Molin, W. Lewandowska-Iwaniak, B. Kusz, M. Gazda, P. Jasinski, J. Electroceram. 28 (2012) 80–87.
[15] C. Lim, S. Sengodan, D. Jeong, J. Shin, G. Kim, Int. J. Hydrogen Energy 44 (2019) 1088–1095.
[16] W. Jung, H.L. Tuller, Solid State Ionics 180 (2009) 843–847.
[17] M. Kuhn, J.J. Kim, S.R. Bishop, H.L. Tuller, Chem. Mater. 25 (2013) 2970–2975.
[18] A. Rothschild, W. Menesklou, H.L. Tuller, E. Ivers-Tiffée, Chem. Mater. 18 (2006) 3651–3659.
[19] F. Schulze-Küppers, S.F.P. ten Donkelaar, S. Baumann, P. Prigorodov, Y.J. Sohn, H. J.M. Bouwmeester, W.A. Meulenberg, O. Guillon, Separ. Purif. Technol. 147 (2015) 414–421.
[20] C.Y. Yoo, H.J. Bouwmeester, Phys. Chem. Chem. Phys. 14 (2012) 11759–11765.
[21] L. dos Santos-Gómez, J.M. Porras-Vázquez, E.R. Losilla, D. Marrero-López, RSC Adv. 5 (2015) 107889–107895.
[22] S.-L. Zhang, D. Cox, H. Yang, B.-K. Park, C.-X. Li, C.-J. Li, S.A. Barnett, J. Mater. Chem. 7 (2019) 21447–21458.
[23] B. Koo, K. Kim, J.K. Kim, H. Kwon, J.W. Han, W. Jung, Joule 2 (2018) 1476–1499.
[24] W. Ni, T. Zhu, X. Chen, Q. Zhong, W. Ma, J. Power Sources (2020) 451.
[25] W. Ni, W. Ma, Q. Zhong, T. Zhu, M. Han, ECS Transactions 91 (2019) 1535–1541.
[26] T. Zhu, H.E. Troiani, L.V. Mogni, M. Han, S.A. Barnett, Joule 2 (2018) 478–496.
[27] V.V. Kharton, A.V. Kovalevsky, A.P. Viskup, J.R. Jurado, F.M. Figueiredo, E. N. Naumovich, J.R. Frade, J. Solid State Chem. 156 (2001) 437–444.
[28] S.-L. Zhang, H. Wang, M.Y. Lu, A.-P. Zhang, L.V. Mogni, Q. Liu, C.-X. Li, C.-J. Li, S. A. Barnett, Energy Environ. Sci. 11 (2018) 1870–1879.
[29] S.-L. Zhang, C.-X. Li, C.-J. Li, J. Power Sources 264 (2014) 195–205.
[30] E. Ksepko, Int. J. Hydrogen Energy 43 (2018) 9622–9634.
[31] M. Izuki, M.E. Brito, K. Yamaji, H. Kishimoto, D.-H. Cho, T. Shimonosono, T. Horita, H. Yokokawa, J. Power Sources 196 (2011) 7232–7236.
[32] J.C. De Vero, K. Develos-Bagarinao, H. Kishimoto, T. Ishiyama, K. Yamaji, T. Horita, H. Yokokawa, J. Electrochem. Soc. 163 (2016) F1463–F1470.
[33] J. De Vero, K.D. Bagarinao, D.H. Cho, H. Kishimoto, K. Yamaji, H. Yokokawa, T. Horita, ECS Transactions 68 (2015) 1943–1952.
[34] V. Dhawan, Y.-C. Huang, D. Dow, R.K. Birla, D.L. Brown, Plast. Reconstr. Surg. 116 (2005).
[35] A. Farlenkov, M. Ananyev, V. Eremin, N. Porotnikova, E. Kurumchin, Fuel Cell. (2014) 15.
[36] Y.L. Liu, A. Hagen, R. Barfod, M. Chen, H.J. Wang, F.W. Poulsen, P.V. Hendriksen, Solid State Ionics 180 (2009) 1298–1304.
[37] S.-L. Zhang, H. Wang, T. Yang, M.Y. Lu, C.-X. Li, C.-J. Li, S.A. Barnett, J. Mater. Chem. 8 (2020) 25867–25879.
[38] M.B. Hanif, J.T. Gao, K. Shaheen, Y.P. Wang, M. Yasir, S.L. Zhang, C.J. Li, C.X. Li, J. Power Sources 472 (2020) 228498.
[39] K. Shaheen, Z. Shah, H. Gulab, M.B. Hanif, S. Faisal, H. Suo, Solid State Sci. 102 (2020) 106162.
[40] K. Shaheen, H. Suo, Z. Shah, M.B. Hanif, Z. Hussain, S. Ali, Y. Wang, Ceram. Int. 46 (2020) 8832–8838.
[41] M.B. Hanif, J.T. Gao, S. Qayyum, K. Shaheen, Y.P. Wang, M. Yasir, C.J. Li, C.X. Li, Ceram. Int. 47 (2021) 10893–10904.
[42] M.B. Hanif, J.T. Gao, K. Shaheen, Y.P. Wang, M. Yasir, C.J. Li, C.X. Li, Int. J. Hydrogen Energy 46 (2021) 8778–8791.